The Skin-Layer Ocean Heat Flux Instrument (SOHFI). Part I: Design and Laboratory Characterization

L. A. SROMOVSKY, J. R. ANDERSON, F. A. BEST, J. P. BOYLE, C. A. SISKO, AND V. E. SUOMI*

Space Science and Engineering Center, University of Wisconsin—Madison, Madison, Wisconsin

(Manuscript received 31 March 1998, in final form 13 November 1998)

ABSTRACT

An untended instrument to measure ocean surface heat flux has been developed for use in support of field experiments and the investigation of heat flux parameterization techniques. The sensing component of the Skin-Layer Ocean Heat Flux Instrument (SOHFI) consists of two simple thermopile heat flux sensors suspended by a fiberglass mesh mounted inside a ring-shaped surface float. These sensors make direct measurements within the conduction layer, where they are held in place by a balance between surface tension and float buoyancy. The two sensors are designed with differing solar absorption properties so that surface heat flux can be distinguished from direct solar irradiance. Under laboratory conditions, the SOHFI measurements agree well with calorimetric measurements (generally to within 10%). Performance in freshwater and ocean environments is discussed in a companion paper.

1. Introduction

The Skin-Layer Ocean Heat Flux Instrument (SOHFI) is being developed for long periods of untended in situ measurement of surface heat flux in an ocean environment. A preliminary description of this work was provided by Suomi et al. (1996). Our long-term objective is a sensor and data collection system that can be deployed from drifting buoys in support of field experiments from which heat flux parameterization algorithms could be refined and tested, and in support of operational measurement programs. Direct and accurate measurements of the heat flux across the air–sea interface has long been a goal for remote sensing, which requires this information to validate measurements made from satellite observations, and to provide a database for improvement of heat flux parameterization schemes used in global climate models. Ocean heat flux forcing is clearly a major factor in the development of circulation systems over the entire globe. Modeling studies have shown that accurate portrayal of surface heat fluxes is critical for simulating such diverse phenomenon as El Niño–Southern Oscillation (ENSO) warm events and rapid coastal cyclogenesis in the eastern United States (e.g., Sanders and Gyakum 1980; Kuo et al. 1991; Emanual 1986, 1991; Black and Holland 1995). In the case of tropical cyclones the major role of surface heat fluxes is obvious since the principal energy source for these systems is the release of latent heat.

Our development effort was strongly motivated by the fact that heat flux measurement techniques currently available are either inaccurate or inconveniently complex, or both. For example, Bradley et al. (1991) note that, while many authors view 10 W m^{-2} as a significant energy input in the context of global change research, uncertainties of the order of 80 W m^{-2} are apparent in the current climatological estimates of the surface mixed layer of the western equatorial Pacific Ocean. They also raise concerns about systematic biases resulting from special weather conditions of that region, for example, frequent rainstorms and extended periods of light winds and convectively driven transports, which may invalidate parameterization schemes developed in other parts of the globe.

The potential advantages of a fully developed SOHFI are significant: direct measurement at the ocean surface, low cost, and simple operation, which facilitates long duration deployment of multiple systems in support of field investigations. It also would address a need for untended solar irradiance measurements; using standard solar radiometers is made difficult by the need to be kept dry and frequently cleaned of salt deposits. SOHFI has no such requirements and is self-cleaning. This system could potentially answer a measurement need that has been recognized for many years in planning for the World Climate Research Program (World Meteorolog-

* Deceased.

Corresponding author address: Dr. L. A. Sromovsky, Space Science and Engineering Center, University of Wisconsin—Madison, 1225 West Dayton Street, Madison, WI 53706.
E-mail: larry.sromovsky@ssec.wisc.edu

ical Organization 1990; The Ocean Observing System Development Panel 1995) but has so far remained unsatisfied by a lack of sufficiently accurate instruments and measurement techniques that could be deployed on the required scale.

In the following we first review the ocean heat flux measurement problem and the characteristics and limitations of prior heat flux measurement techniques. We next review current understanding of heat flux within the surface skin layer, followed by a description of the SOHFI sensor design, which is based on skin-layer measurements. We next present the results of preliminary laboratory tests, followed by an assessment of the current state of SOHFI development and performance. In a companion paper (Sromovsky et al. 1999), which we will hereafter refer to as Part II, we describe the results of field testing of SOHFI.

2. The air–sea heat flux measurement problem

a. Basic components

The total heat flux from the ocean to the atmosphere can be written as follows:

$$H_T = H_S + H_E + H_R + H_P - H_{\text{Sun}}, \qquad (1)$$

which shows the net heat loss as the sum of sensible (H_S), evaporative (H_E), thermal radiative (H_R), and precipitation losses (H_P), less the shortwave solar energy absorbed (H_{Sun}). (Here we ignore the transports by spray.) The sensible, evaporative, and precipitation heat exchanges occur at the air–sea interface, while thermal radiative exchanges occur within about 50 μm of the surface (McAlister and McLeish 1969). Only shortwave radiative exchanges occur over an extended depth. According to the solar absorption model of Paulson and Simpson (1981), based on data from Defant (1961), about 13% of incident sunlight is absorbed within the top millimeters of the surface, but only 25% of it is absorbed within the first centimeter.

The net transfer of thermal radiation from the ocean surface to the atmosphere can be approximated as

$$H_R = \epsilon(\sigma T_s^4 - H_{\text{LW}}), \qquad (2)$$

where H_{LW} denotes the incident downwelling longwave radiation, ϵ is the effective emissivity of the surface, T_s is the surface temperature, and σ is the Stefan–Boltzmann constant. Schluessel et al. (1990), using refractive index values from Downing and Williams (1975), computed effective emissivities of 0.886 at 280 K and 0.89 at 300 K. This calculation weights the spectral variation of surface emissivity by the blackbody radiance spectrum but assumes a flat ocean surface. However, because surface roughness and thus emissivity both depend on wind speed (Masuda et al. 1988), and because the spectrum of downwelling and upwelling thermal radiation fluxes are often considerably different, the above characterization is probably uncertain by several percent over a typical range of conditions. Measurement of the downwelling long-wave flux is a nontrivial matter under open ocean conditions, where some tending is required to keep sensor windows clean and dry. By integrating this component of the flux into one combined measurement, our sensor avoids these complexities.

Solar radiation is a highly variable and generally large component that needs to be measured accurately to keep its uncertainty from dominating all others. Accurate instruments for solar measurement, such as Eppley pyranometers, also need cleaning and tending. Part of the downwelling solar radiation is reflected from the surface, thus transferring no heat, and part of the light entering the surface is subsequently scattered out of the ocean without being absorbed. Without short wavelength upwelling measurements, a model of the ocean albedo is needed to account for these effects. Schluessel et al. (1990) used tabulated values of albedo given by Payne (1972) and computed the net solar radiation as

$$H_{\text{Sun}} = (1 - a)H_D, \qquad (3)$$

where H_D is the downward solar flux, and the albedo (a) is a function of wind speed and angle of incidence. Because it is essentially the net solar radiation that is sensed by our in situ sensor, these latter effects need not be considered in the heat input equation, except during calibration, which does rely on external measurements.

b. Prior methods of measuring turbulent transports

Most current methods of determining turbulent fluxes (sensible and latent heat components) rely on measurements within the atmosphere above the ocean surface. The four principal methods that have seen extensive use are 1) eddy correlation, 2) dissipation, 3) profile, and 4) bulk aerodynamic. Practical limitations of these methods for experiments requiring more than a few days duration were reviewed by Blanc (1983b). The key characteristics and practical limitations are briefly reviewed and updated in the following.

The eddy-correlation method is a direct model-independent technique that measures the covariance of vertical velocity fluctuations with fluctuations in temperature and humidity. Rapidly responding temperature and humidity sensors are able to capture the fluctuations in these parameters on the scale size of eddies as small as 1 to 10 m (Larsen et al. 1980; Hay 1980). However, some of these sensors are susceptible to salt contamination and require frequent cleaning, and most could not be used in rain, wet snow, or heavy fog. The most widely used rapidly responding humidity sensor (the Lyman-alpha hygrometer) is affected by rapid deterioration of UV windows that results from exposure to moist air, salt contamination, or precipitation. More recently, for measurement of wind and temperature fluctuations, sonic anemometers appear to be the best solution to the salt contamination problems (Schotanus et

al. 1983; Fairall et al. 1990). For measurement of rapid humidity fluctuations, a dual-wavelength infrared sensor has shown promise, though this remains a difficult measurement issue (Edson et al. 1998). An additional complexity of the eddy-correlation method is the need for correction of ship motions (Mitsuta and Fujitani 1974; Edson et al. 1998). While this technique has the considerable virtue of providing direct measurement of the quantities of interest and has become more practical recently, it is still challenging to carry out, especially for long periods under variable and severe environmental conditions.

The dissipation method uses an empirical relationship between heat fluxes and the spectrum of one-dimensional fluctuations of wind speed, temperature, and humidity. This method needs even more rapidly responding and smaller sensors than are required for the eddy-flux method, and are thus even more sensitive to salt contamination. It is relatively insensitive to ship motions but requires independent information to define the heat flux direction. Also, the range of conditions for which this technique can be considered valid still needs to be established (Dobson et al. 1980).

The inertial dissipation method is a variant that sidesteps the high-frequency measurement problem by measuring turbulence spectra in the lower frequency inertial subrange of isotropic turbulence, where more rugged sensors such as sonic anemometers can be used (Larsen et al. 1993). In this approach, the so-called Corsin relations are used to determine dissipation variables from which the fluxes can be computed (Fairall and Larsen 1986). Fairall et al. (1990) describe a practical real-time shipboard inertial dissipation measurement system that agreed with eddy-correlation measurements to within root-mean-square differences of 25%.

The profile method is semiempirical in nature, using measurements of wind speed, temperature, and humidity at multiple levels. Differential quantities (vertical gradients) are used to estimate the vertical fluxes using coefficients derived from empirically derived flux-profile relationships (Dyer 1974), but according to the analysis of Blanc (1983a) this method has a high sensitivity to instrumental errors.

The bulk aerodynamic method computes turbulent fluxes using empirical functions of sea surface temperature, wind, temperature, and humidity at a single atmospheric reference level (usually 10 m). Following Kraus (1972), Fleagle and Businger (1980), Guymer et al. (1983), and Kraus and Businger (1994), we write the bulk aerodynamic equations for heat and momentum transport in the following form:

$$H_S = \rho_a C_S C_P U(T_s - \theta), \tag{4}$$

$$H_E = \rho_a C_E L U(q_s - q), \quad \text{and} \tag{5}$$

$$\tau = \rho_a C_D U^2, \tag{6}$$

where τ is the surface wind stress; T_s is the surface temperature; $\theta = T + 0.0098z$ is the potential temperature at the reference level z; q_s and q are specific humidities (kg of water vapor per kg of air) at surface and reference levels, respectively; ρ_a is the density of air; C_p is the specific heat at constant pressure; L is the heat of vaporization; and U is the mean wind speed at the reference level measured relative to the surface current. The dimensionless bulk aerodynamic transfer coefficients are C_S for sensible heat, C_E for evaporative flux, and C_D for wind stress. The specific humidity q_s for saltwater is 98% of the saturation specific humidity of freshwater at the sea surface temperature.

The bulk aerodynamic method is particularly valuable in preliminary validation of SOHFI because it uses measurements that are more readily available in the field. However, to apply these equations over a wide range of atmospheric conditions requires accounting for the dependence of the transport coefficients on wind speed and stability. The semiempirical similarity theory providing the basis for this is described by Businger et al. (1971) and Liu et al. (1979). A thorough discussion of these and other effects incorporated in the Coupled Ocean–Atmospheric Response Experiment 2.0 (COARE 2.0) bulk algorithm is provided by Fairall et al. (1996). A relatively simple formulation that accounts for the most significant dependencies is provided by Kondo (1975) and applied in Part II.

c. Measurement problems

As pointed out by Blanc (1983b), all of these methods suffer, to some degree, from perturbations by the measurement platforms. This is especially serious for shipboard observations since even upwind measurements can be influenced by the ship for distances comparable to the windward cross section of the ship (Mollo-Christensen 1979).

Large differences between various schemes have been a common occurrence. Blanc (1983a) evaluated 20 different schemes and found flux values that differed by more than 100% for the same input temperature, humidity, and wind data. Donelan (1990) argues that applying a simplified similarity theory to complex marine boundary layers can be problematic because of larger-scale motions that decouple the various fluxes from the local system. Reliable measurements, such as those accomplished by eddy correlation, are very rare under a wide range of atmospheric or oceanic conditions (Blanc 1983b). On the other hand, Fairall et al. (1996) report very impressive agreement between COARE 2.0 bulk calculations, dissipation measurements, and eddy-flux measurements. This encouraging result offers hope for meaningful intercomparisons over extended time periods and weather conditions without costly deployments of eddy-correlation systems.

The previously discussed methods for measuring turbulent fluxes generally perform poorly at very low wind speeds, partly because of sensor limitations. The bulk

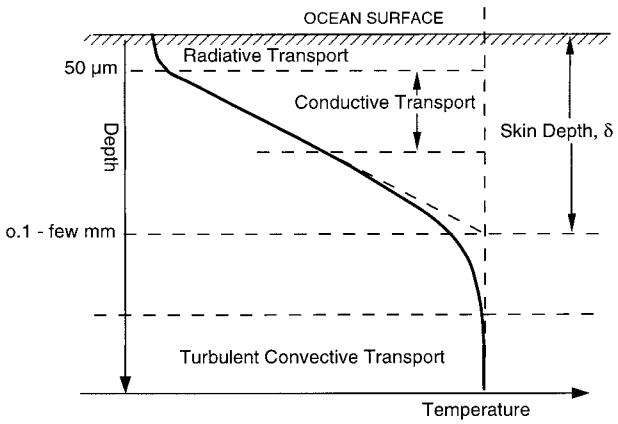

FIG. 1. Illustration of heat transport regimes near the surface of the ocean. The skin depth δ is the intersection point of the projected linear conductive temperature gradient and the projected isothermal profile from the turbulent convective regime.

transfer equations also require large coefficient corrections at small wind speeds, and their implication that transport is zero when the mean wind is zero is not accurate. For example, Bradley et al. (1991) measured fluxes of 25 W m^{-2} under zero wind conditions, a transfer powered by free convection rather than by turbulence associated with the mean flow. The COARE 2.0 algorithm (Fairall et al. 1996) deals with the low wind speed problem by incorporating a gustiness factor. The low wind speed regime is just where our sensor probably provides the best performance and thus presents a good opportunity to help the development of parameterization schemes to deal properly with light wind heat transport conditions.

3. The nature of skin-layer heat flux

The temperature profile of the ocean surface layer is schematically shown in Fig. 1. Between the top 50 μm, where thermal radiation exchange takes place, and the deeper, nearly isothermal, region where convective turbulent transport occurs, is a region where transport is purely by thermal conduction. The conductive region is characterized by a linear temperature gradient proportional to the transported heat flux.

It is usual to define a characteristic thickness of the conduction sublayer as (e.g., Paulson and Simpson 1981)

$$\delta = \frac{K(T_b - T_s)}{H} = \frac{K\Delta T}{H}, \tag{7}$$

where T_b is the bulk water temperature below the cool skin layer, H is the net heat flux, and K is the thermal conductivity of water. This is the depth at which the extrapolated linear temperature profile of the conduction region intersects the nearly constant temperature of the deeper turbulent region, not the actual thickness of the linear layer. It appears from limited direct measurements, however, that the linear region is a sizable fraction of δ (Mammen and von Bosse 1989). This layer varies from millimeters to fractions of a millimeter, decreasing with increasing wind speed.

The existence of a sublayer in which heat transfer is primarily by molecular conduction was verified by Khundzuha et al. (1977). Their measurements of temperature gradients across the surface of the Black Sea revealed a layer that is 0.2–0.6 mm thick in which a linear temperature gradient existed for winds up to 6–8 m s^{-1}. The heat flux they computed using

$$H = K\frac{dT}{dz} \tag{8}$$

agreed to within 10% with the turbulent heat transfer measured independently at a depth of 20 cm. According to Haussler (1956), for convectively driven turbulence with heat fluxes comparable to typical ocean values, laboratory measurements showed a linear temperature profile to depths of 1–2 mm. For wind-driven turbulence, McAlister and McLeish (1969) estimate that the linear region is only about 0.4 mm deep for wind speeds of 10 m s^{-1}. However, this estimate is for a solid boundary with the same stress as the free boundary. They argue that for a free boundary less of the stress will be seen in surface currents, so that the laminar layer will be somewhat thicker. Linear temperature profiles were also measured by Mammen and von Bosse (1990), using a rapidly responding fine platinum resistance thermometer that was plunged through the surface from below. They provided sample measurements showing 3–5-mm linear regions under conditions of small heat fluxes but found a very sharp gradient within the upper 0.5 mm at a wind speed of 10 m s^{-1}.

On dimensional grounds Saunders (1967) proposed that the skin depth should satisfy

$$\delta = \frac{\lambda\nu}{(\tau/\rho)^{1/2}} = \frac{\lambda\nu}{U_{*w}}, \tag{9}$$

where λ is an empirically derived constant, ν is the kinematic viscosity of water (1.005×10^{-6} m^2 s^{-1} at 20°C), ρ is the density of water, τ is the surface stress, and $U_{*w} \equiv (\tau/\rho)^{1/2}$ is the friction velocity in the water. The friction velocity in air is defined by $U_* \equiv (\tau/\rho_a)^{1/2}$, where ρ_a is the density of air. This can be expressed in terms of wind speed under neutral stability conditions using the log wind profile and Charnock's relation (Charnock 1955) to implicitly define U_* as a function of U:

$$\frac{U}{U_*} = \left(\frac{1}{k}\right)\ln\left(\frac{z}{z_o}\right) \quad \text{and} \tag{10}$$

$$z_o = \frac{\alpha U_*^2}{g}, \tag{11}$$

where z_o is the aerodynamic roughness length, k is the

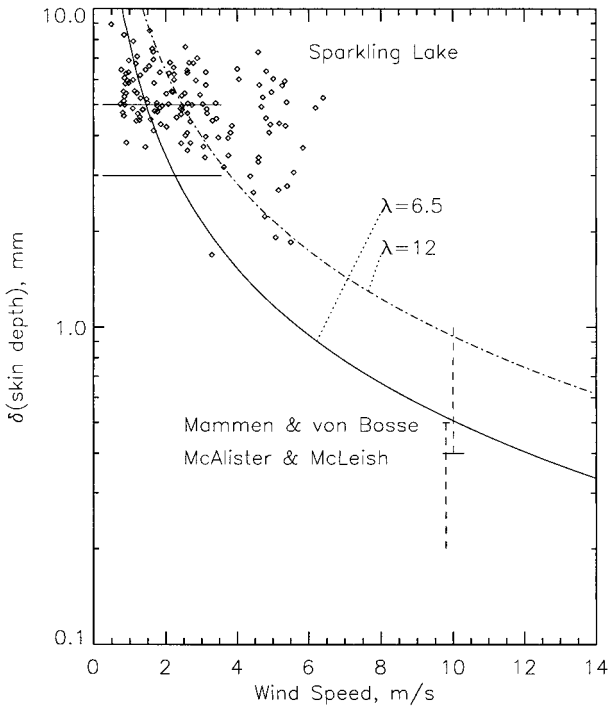

FIG. 2. Skin depth as a function of wind speed at 10 m: continuous curves are for the Saunders (1967) relation with $\lambda = 6.5$ for open ocean conditions and $\lambda = 12$ for low-fetch conditions; points indicate Sparkling Lake results. The horizontal lines at 3 and 5 mm indicate low flux results of Mammen and von Bosse (1988). Dashed vertical bars near 10 m s^{-1} extend upward from the lower bound of McAlister and McLeish (1969) and downward from the upper bound of Mammen and von Bosse (1988).

von Kármán constant (generally taken to be 0.4), and α is a constant taken to be 0.016 (Stull 1988). Once U_* is determined, U_{*w} can be computed as $U_*(\rho_a/\rho)^{1/2}$ and then substituted into Eq. (9) to obtain the corresponding skin depth. The computed wind speed dependence is shown in Fig. 2 for $\lambda = 6.5 \pm 0.6$, derived from measurements on the open Pacific north of Hawaii in 1974 by Paulson and Simpson (1981), and for $\lambda = 12$, a value more typical of laboratory or short-fetch conditions (Paulson and Parker 1972; Hill 1970).

During the Sparkling Lake deployment of an early version of the SOHFI, discussed in detail in Part II, we obtained approximate estimates of the conduction sublayer thickness using the measured heat flux and the difference between the surface and the 1-cm temperatures in Eq. (7). As the wind speed at the 2-m level increased from 1 to 6 m s^{-1}, our estimate of δ decreased from about 6 to about 3 mm (Fig. 2). These crude results have about the right value at low wind speeds, but do not decrease as rapidly as expected with increasing wind speed, perhaps because the assumed neutral-stability wind profile was not satisfied for these measurements.

The basic SOHFI measurement approach is to place a thin heat flux sensor within the conductive region of the skin layer so that the total heat transport can be monitored. If the sensor is thin enough, or has thermal conductivity close to that of the water it displaces, then its presence should not significantly alter the heat flow to be measured. Of course, this simplified view neglects the fact that the sensor presents a local barrier to viscous coupling of fluid immediately above and below it and thus could alter the turbulence and temperature structure below this laminar region. The sensor also presents a barrier to surface renewal events that penetrate the laminar layer (Liu and Businger 1975). In both cases, however, it is not clear whether these local perturbations of the surface environment would lead to substantially different heat fluxes. In fact, limited intercomparison measurements presented in the following suggest that they do not.

In the next section we describe our new instrument (SOHFI), which is distinct from all previously described heat flux measurement techniques in the following ways: 1) it makes direct measurements of flux within the ocean rather than above it; 2) it responds to all flux components, eliminating the need for auxiliary measurements; 3) it separately measures solar flux; 4) it has the potential for remote untended operation for long time periods; and 5) its design is inherently well suited for operation at low or zero wind speeds.

4. Instrument design

The current SOHFI employs a modification of a commercial thin-film heat flux sensor held in the cool skin layer of the ocean by surface tension acting on a woven fiberglass membrane supported by a low-mass, ring-shaped, wave-following float. Our drifter instrument package (Fig. 3) uses a World Ocean Circulation Experiment (WOCE)-type Lagrangian drifter buoy (Sybrandy and Niiler 1991) to provide flotation and resistance to wind drift. A 25-ft floating cable connects the sensor float to the buoy, which contains batteries, the signal processing electronics, and a Telonics transmitter for communication with the Argos satellite data collection system. The most important element of this system, the flux plate sensor, will be described first.

a. Flux sensor description

The heat flux sensor we used initially was a standard commercial flat plate flux sensor (Ortolano and Hines 1983). Later versions employed special modifications to improve resistance to saltwater invasion. The flux sensor is constructed as a thin sandwich (Fig. 4), the central component of which is a thermal resistor made from a thin sheet of plastic; 0.000 92-in. (0.0234-mm) Mylar is used for the current configuration. A 40-junction differential thermopile is made from 0.0002-in. (0.0051-mm) thick edge-bonded constantan and Chromel foils that are etched to form a serpentine pattern of alternating junctions (Fig. 4b). The thermal resistor is threaded through the foil pattern so that alternate ther-

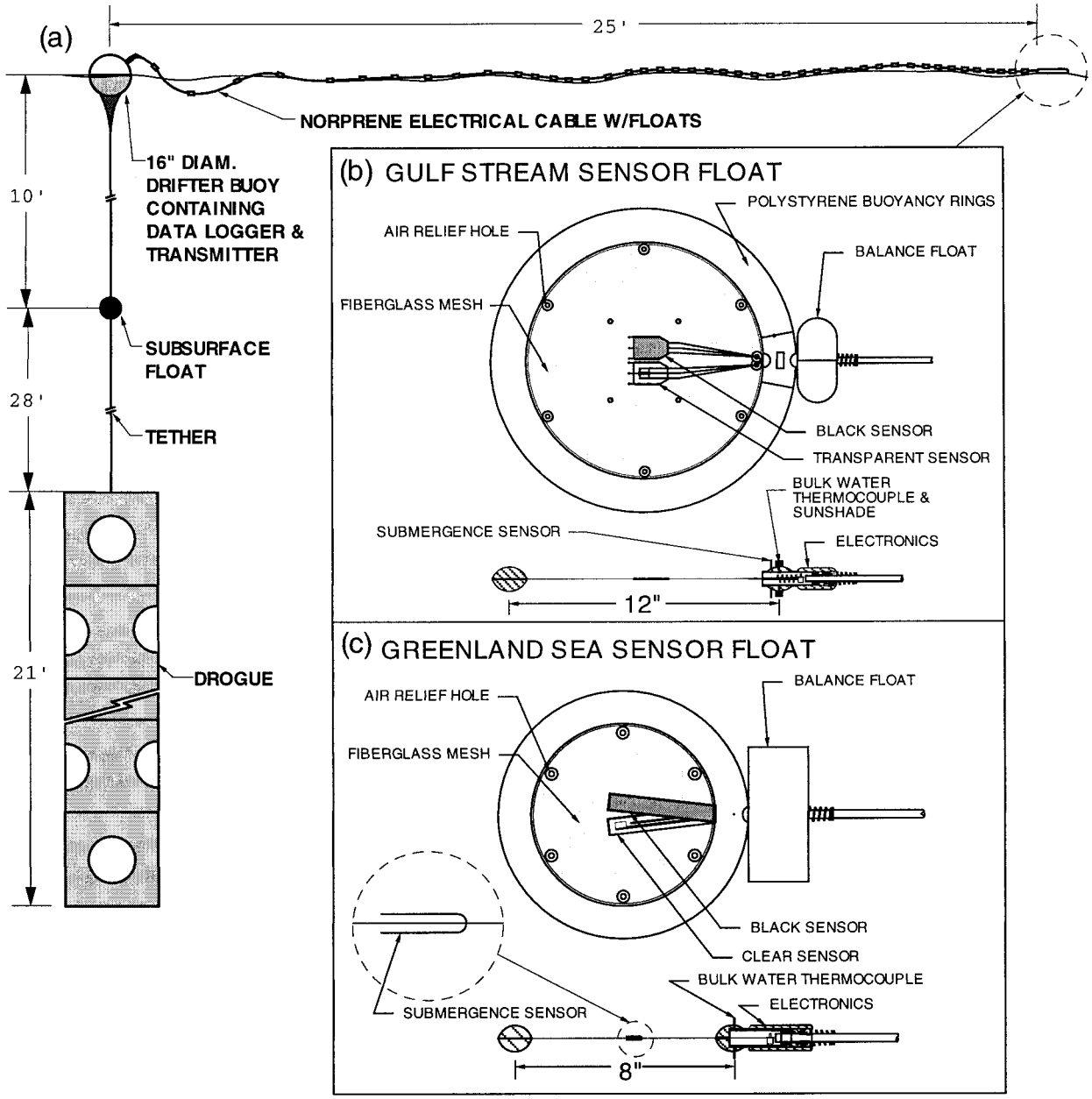

FIG. 3. SOHFI drifter configuration for field measurements: (a) Lagrangian drifter package with buoy and surface sensor float, (b) detailed top view of sensor float construction used in early Gulf Stream deployment, and (c) detailed view of a revised sensor float design used in the Greenland Sea deployment. The referenced deployments are discussed in Part II. Bird countermeasures are not shown.

mocouple junctions are positioned on opposite sides of the resistance sheet. After copper ribbon leads are attached, outer sheets of protective plastic are bonded on each side of the sandwich. Also bonded within the sandwich is a Chromel–constantan foil thermocouple for sensing the skin temperature. In earlier deployments we used a dual-thermopile configuration with wire leads (Fig. 4c). Our current configuration (Fig. 4d) uses a single-thermopile element (per detector) and ribbon leads to provide greatly increased resistance to saltwater invasion. In our very first field deployment we used a sensor configuration as in Fig. 4c, but the sandwich had two more layers than are shown in Fig. 4a, consisting of top and bottom covers of aluminized Mylar.

Heat flowing normal to the plane of the flux sensor generates a temperature difference across the thermal resistor, inducing a thermopile output voltage given by

$$V(H, T) = \frac{n_{jp}\alpha_{cc}(T)y_r H}{K_r(T)} = R(T)H, \qquad (12)$$

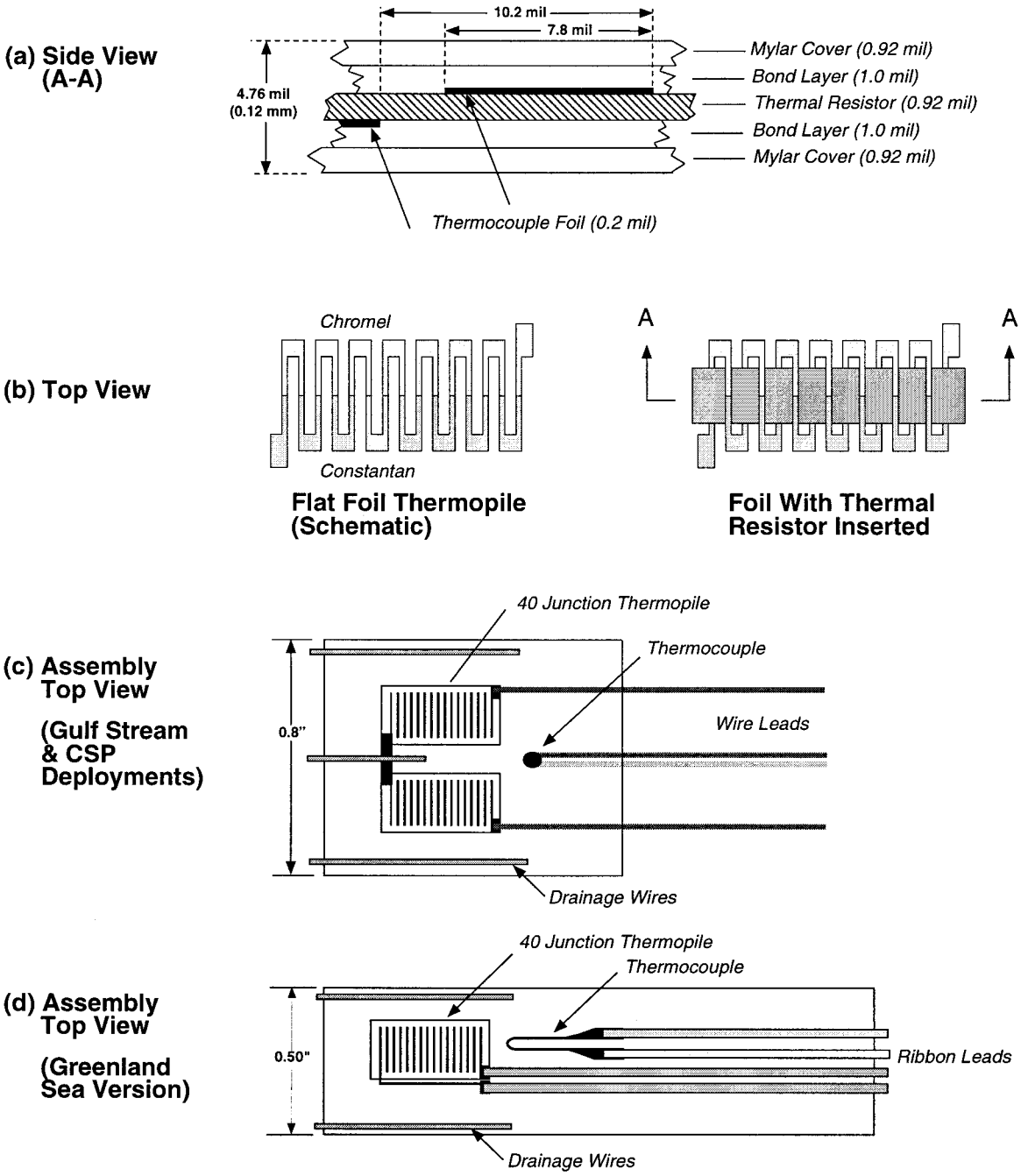

FIG. 4. SOHFI flux sensor configuration: (a) cross-sectional view of sensor layer, (b) top view of thermopile junction layout, (c) top view of assembled flux plate sensor used in early ocean tests, and (d) revised design using improved construction techniques.

where n_{jp} is the number of junction pairs, α_{cc} is the Chromel–constantan Seebeck coefficient defining the voltage output per junction pair per unit temperature difference, y_r is the thermal resistor thickness, K_r is the thermal conductivity of the resistance material, H is the heat flow normal to the plane of the sensor, and R is the responsivity. Our current design has a total package thickness of about 0.0047 in. (0.12 mm), including two 0.001-in. bonding layers and three layers of Mylar film. The thermal resistor and protective layers are all made of DuPont 92d Mylar, with a nominal thickness of 0.92 mils (0.0234 mm) and a tolerance range between 0.95 and 0.88 mils (0.0241 and 0.0224 mm). Note that the assembled sensor is considerably thinner than the conduction layer under most conditions (Fig. 2).

Given parameter values of $n_{jp} = 20$ (Fig. 4d), $\alpha_{cc}(20°C) = 60.5$ mV °C^{-1}, $y_r = 2.34 \times 10^{-5}$ m, and $K(20°C) = 0.15$ W (m °C)$^{-1}$, the responsivity of the

flux plate should be 0.189 μV (W m^{-2})$^{-1}$, with a tolerance range of 0.180–0.195 μV (W m^{-2})$^{-1}$, considering only the tolerance of the resistance layer thickness. This compares well with the manufacturer's calibration of the flux sensors, which is typically in the range of 0.181–0.197 μV (W m^{-2})$^{-1}$. Calibration uncertainty contributes 3%–5% to this variation (Ortolano and Hines 1983), with the rest presumably coming from material and assembly variations. The sensor's responsivity has a weak temperature dependence of about 0.14% °C^{-1} near 20°C, due primarily to the 0.16% °C^{-1} dependence of the thermoelectric coefficient.

Although the signal output from this thermopile is rather small, only about 2 μV for a climatically significant 10 W m^{-2}, preamplifier noise only contributes about 0.2 μV Hz$^{-1/2}$, so that for a 20-min average (with a bandwidth of 0.0008 Hz) the main source of random noise is due to the fluctuations in the heat transfer process itself. However, the low responsivity of the sensor does present an offset problem. While the thermopile reverses sign with the direction of heat flow and has a natural zero offset when no heat is flowing, the preamp does have an input offset that varies from lot to lot, and with temperature, but is typically of the order of a microvolt. The flux equivalent offset is about 5 W m^{-2} for the thermopile parameters listed above and can be reduced by increasing the number of junctions or by increasing the thermal resistance layer thickness. Such design modifications would be particularly useful in dealing with the larger offsets seen at low preamp temperatures and lower power supply voltages (discussed in Part II). As discussed in a subsequent section, there are also data analysis techniques that can correct for offsets.

Because the thermal conductivity of water [0.606 W (m K)$^{-1}$ at 295 K] is about four times that of Mylar, the temperature drop across the flux plate is about four times what would be seen in the equivalent thickness of water. But even for a flux of 500 W m^{-2} that difference only amounts to 0.32 K.

b. The sensor float assembly

The key design feature of the sensor float is the use of surface tension acting against buoyancy to hold the flux plate detector within the conductive skin layer. As illustrated in Fig. 3, the flux plate sensors are bonded between sheets of fiberglass mesh held in tension by a ring-shaped wave-following float, 8–12 in. in diameter. The float and sensors are designed with a high degree of symmetry to facilitate operation in either top-up or top-down orientations. This capability is needed because the float flips over many times during extended periods of moderate to high wind conditions. The buoyancy of the float is adjusted so that, under dead calm conditions, it would initially suspend the sensor several millimeters above the water surface. But once part of the mesh touches the water, surface tension pulls the mesh layers into firm contact with the surface, wets the sensor, and also serves to dampen small capillary waves within the area covered by the mesh. Surface tension is so effective that pulling the float out of the water requires a force several times the weight of the float. Good wave-following characteristics are assured by having a low profile disc-shaped float that has low mass and high differential buoyancy for small displacements. Small size is helpful in following smaller and more sharply curving wave profiles. The excellent wave-following characteristics were observed during various deployments in different sea state conditions. Nevertheless, waves with sharply curved profiles can result in the temporary loss of mesh contact with the surface, allowing penetrations of water above the surface. When the sensor is at wave crest, high winds can also blow the sensor off the top of the wave, resulting in possible overturning, which can also happen as a result of breaking waves. As described later, we have implemented sensors that allow at least partial filtering and/or correction for these events.

The fiberglass mesh is a woven cloth with 50 threads per inch in the warp (lengthwise) direction, with each multifilament thread comprising 204 5-μm filaments, and 20 threads per inch in the woof (cross thread) direction, using 104 5-μm filaments for these threads. The measured thickness of the mesh is about 1.7 mils (0.043 mm). Fiberglass was chosen initially for its dimensional stability, its transparency to solar radiation, and its good wetting and surface tension characteristics. However, if the mesh is placed in direct contact with the flux plate, its interlocking threads impeded water flow and diffusive exchange across the thermopile, so that under strong evaporative fluxes the salt concentration immediately above the flux plate increases with time following exposure. This produces a local decrease in the saturation vapor pressure and a significant gradual decline in the thermopile signal. We were able to eliminate this response droop by inserting spacers, termed ''drainage wires,'' between the mesh and the flux sensor, so that salt concentrations could diffuse before they reached levels that could affect evaporation rates (Fig. 5). We currently use drainage wires with a 20-mil outer diameter (0.51 mm); two are placed on each side of each flux sensor, as indicated in Figs. 4 and 5. The droop effect was uncovered in laboratory tests and defeated prior to any saltwater deployments. It was not present in freshwater lake deployments. In the first freshwater deployment at Sparkling Lake (described in Part II), no drainage wires were used, and none were needed.

The float includes a mercury switch to sense which side is facing up so that the proper sign can be attached to the observations. Because the orientation can reverse within the 20-min averaging period, decommutation (polarity correction) of the flux signals is required prior to averaging. When offsets are present in the preamplifier, frequent reversals of float orientation have the beneficial effect of reducing the offset contribution. In

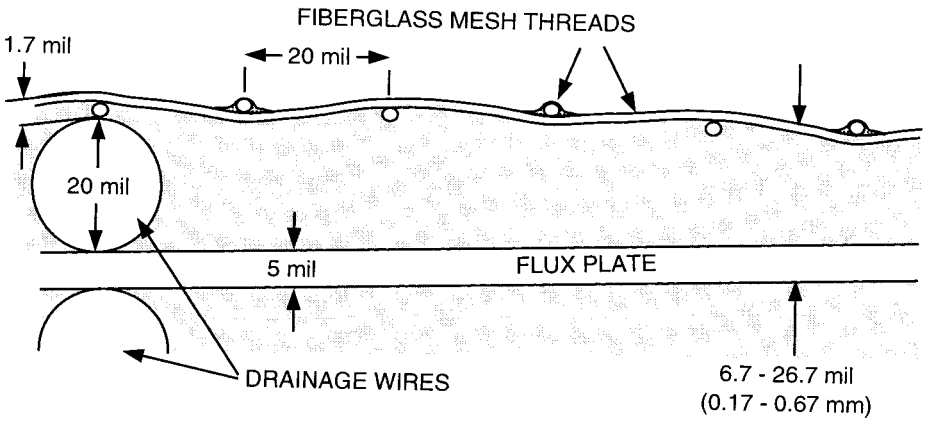

FIG. 5. SOHFI sensor interface to the ocean surface. Surface tension on the fiberglass mesh maintains contact with the surface. Drainage wires shown in cross section maintain a small gap between the flux plate and the mesh. This gap is needed to diffuse salt concentrations produced by evaporation.

fact, if the float spends equal time in both orientations, then the offset contribution is identically zero. Even if the time spent is not equal, because the fractional time in each orientation is measured, it becomes possible to correct for offsets that are slowly varying, as discussed in the following section.

The float is also equipped with submergence sensing capability. When the resistance between two bare metal pins, one below and one above the nominal waterline, falls below a threshold value, the float is considered submerged, and data samples during such times are omitted from the 20-min averages. This is needed because the thermopile signal is invalid, and usually near zero, when it is not in the skin layer. We are still investigating how best to design the submergence pins so that they detect the most relevant information. The latest design places them close to the flux sensors, only a few millimeters above and below the mesh surface. Our earliest design had them located on the ring-shaped float (both designs are illustrated in Fig. 3). A comparison of submergence-filtered flux averages with unfiltered averages shows that the filtering does increase the measured flux values during periods of frequent submergence, although we cannot yet be sure what fraction of the submergence-induced signal depression is removed by the filtering.

Experience with seabird attacks in two of three ocean deployments (Part II) motivated several design changes. The foam ring material was made stronger by using divinylcell, a structural PVC foam, instead of polystyrene. The ring was painted gray for camouflage, and a more rugged flux plate was developed (Fig. 4d). Following the advice of wildlife experts, we have also been experimenting with the use of projecting spines to make the sensor float look less attractive to the seabirds. These are made of sharpened carbon fiber rods embedded in the foam ring.

c. Signal processing and offset corrections

While the thermopile is inherently symmetric in response, the overlying mesh has the potential to modify the local heat transport in the immediate vicinity of the thermocouple junctions. Because the flux sensor sandwich is so thin, and the junctions region is so narrow, the response of the sensor is actually highly localized to the region of the junctions. If some of the junctions happen to be directly beneath fiberglass mesh fibers, they will be partly shielded from the airflow that transports heat across the surface. Thus, it is reasonable to expect some slight variation in response between normal (top up) orientation and the reverse orientation (top down). Accounting for this effect, and a preamplifier input offset voltage V_{off}, the most general equation relating surface heat flux H to input-referenced signal voltage, is given by

$$\text{top up:} \quad V = R^u H + V_{\text{off}} \quad \text{and} \tag{13}$$

$$\text{top down:} \quad V = -R^d(-H) - V_{\text{off}}, \tag{14}$$

where the superscripts u and d refer to top-up or top-down orientations, respectively. Note that in the second equation, both thermopile and input offsets are shown reversed by the decommutation operation that is triggered by the mercury switch, as described previously. We used input-referenced voltages (output voltage divided by electronics gain) to allow the responsivity R to retain the same meaning as in Eq. (12).

In general, during the 20-min averaging period that is used to assemble one field measurement, the sensor will spend some time in both orientations. We can write the general average in the form

$$V_i = (f_{u,i}R^u + f_{d,i}R^d)H_i + (f_{u,i} - f_{d,i})V_{\text{off},i} + e_i, \tag{15}$$

where $f_{u,i}$ and $f_{d,i}$ are the fractions of time spent in the up and down orientations (which sum to unity), H_i is the true average heat flux during the averaging period,

and e_i is a random error associated with the ith measurement. The error term is the combined effect of electronics noise and the statistical fluctuation in the heat flux transfer process. If we ignore the small difference between up and down responsivities, and write $R^u = R^d = R$, then the signal equation simplifies to the form

$$V_i = RH_i + (2f_{u,i} - 1)V_{\text{off},i} + e_i. \tag{16}$$

Because the offset is mainly a function of electronics temperature and supply voltage, it is generally slowly varying. This characteristic makes it possible to determine the offset from an analysis of successive measurements. Taking the difference between the two successive measurements, and assuming $V_{\text{off},i} = V_{\text{off},i-1} = V_{\text{off}}$, we find that

$$V_i - V_{i-1} = R(H_i - H_{i-1}) + 2(f_{u,i} - f_{u,i-1})V_{\text{off}} + (e_i - e_{i-1}). \tag{17}$$

For periods when the true heat flux is not systematically increasing or decreasing, which is generally restricted to nighttime conditions, the difference between successive averages of the true flux will have a zero expectation value, as will the difference in the two error terms. Thus, when orientation fractions vary between adjacent samples, fitting the left-hand side of the above equation to a linear function of $f_{u,i} - f_{u,i-1}$, will yield a slope $m \approx 2V_{\text{off}}$, which can then be used to correct the measured averages, and convert the signal voltage to measured heat flux units using

$$H_{\text{meas}} = \frac{[V - (f_u - 0.5)m]}{R}, \tag{18}$$

which should produce, within errors, the same value for both clear and black sensors under nighttime conditions (the design and role of clear and black sensors are described in the following section). The ratio of the results for these two sensors provides a correction factor for adjusting their relative responses to conducted heat fluxes, an important adjustment needed to provide the best solar flux corrections.

d. Sunlight measurement and corrections

The prototype sensor used in the first freshwater deployment had a reflecting coating intended to reduce perturbations by absorbed sunlight. However, by allowing the heating of water directly above the flux plate, but blocking the heating that would otherwise occur directly below the flux plate, even a perfectly reflecting coating still produces a perturbed temperature gradient that causes a depression in the upward flux reading. Subsequently, we made two design modifications to address this problem. First, we changed the flux plate plastic materials from a yellow-brown Kapton to transparent Mylar and removed the reflective covering, allowing sunlight to strike both the top and bottom junctions simultaneously, made possible by the horizontal offset of the upper and lower junctions. Thus, radiation directly absorbed by the junctions would produce no first-order effects because the signals would cancel. Furthermore, water just above and water just below the flux plate would both be exposed to solar heating, allowing the mean temperature to increase with less distortion of the thermal gradient. However, there is still a local depression of solar heating just below the junction region because the thermopile junctions block 76% of the incident sunlight (see Fig. 4a), so that a substantial perturbation of the gradient is still possible. In addition, a much smaller temperature gradient perturbation is produced by absorption within the Mylar.

To deal with these residual solar perturbations and to also allow measurement of the incident sunlight, we included a second flux sensor of identical design except for the use of blackened outer layers of dyed Mylar instead of clear Mylar. The readings of these two sensors of differing solar sensitivity can be extrapolated to obtain a reading with essentially zero solar perturbation. This makes possible both day and night operation and also provides information about possible fouling of the primary sensor that might increase its solar absorption.

The clear and black sensor upward heat flux readings, H_{clr} and H_{blk}, are assumed to be linear functions of true heat flux H and net downward solar flux H_{Sun}, as given by

$$H_{\text{clr}} = H - k_c H_{\text{Sun}} \quad \text{and} \tag{19}$$

$$H_{\text{blk}} = H - k_b H_{\text{Sun}}, \tag{20}$$

where $k_c \approx 0.2$ and $k_b \approx 0.5$ are solar response constants that must be determined by calibration (to be discussed later). Solving for the unknowns as a function of the measurements, we obtain

$$H_{\text{Sun}} = \frac{(H_{\text{clr}} - H_{\text{blk}})}{(k_b - k_c)} \quad \text{and} \tag{21}$$

$$H = \frac{[H_{\text{clr}} - (k_c/k_b)H_{\text{blk}}]}{(1 - k_c/k_b)}. \tag{22}$$

Note that the derived value for the true heat flux depends only on the ratio of k_c to k_b and not on their absolute values. A limitation of the above equations is that they do not account for the wavelength-dependent absorption characteristics of both water and flux plate materials. This is potentially significant because a nonflat spectral response, combined with variable spectral content in the downward solar flux, can lead to different output signals for the same total incident flux. Thus, this factor needs to be considered in establishing correction uncertainties, even though we have not yet seen obviously large errors that can be attributed to spectral variations. Spectral variability in response makes laboratory calibration difficult because accurate simulation of the solar spectrum is required to obtain an appropriate calibration. For this reason, we have preferred to use the far more accurate field calibrations.

To carry out a solar calibration in the field, we first make small differential adjustments in the conductive heat calibrations of the black and clear sensors to make them agree during nighttime conditions, while still maintaining the average calibration. The black − clear difference can then be used with an independent solar flux reference to determine the response difference $k_b - k_c$ using Eq. (21). The solar reference can be a downward flux measurement using a nearby surface or ship-based instrument; usually one or more relatively clear days of intercomparison are needed to allow for different timing of signal modulations produced by cloud shadows. In clear weather, it is also possible to obtain an approximate calibration using a model solar flux, predicted from the geometry and a typical atmospheric optical depth. A comparison of these two methods will be discussed later. Both procedures assume a constant solar spectral content, or a spectrally flat sensor response, neither of which is valid to high accuracy. Nevertheless, because the diurnal variation of solar irradiance is well tracked, the errors of this assumption do not appear to be very large.

To correct for the solar perturbations of the heat flux measurements, we need to determine the k_c/k_b ratio, either by making a determination of one absolute response coefficient [in addition to the $k_b - k_c$ difference derived from Eq. (21), as described above] or by making a direct determination of the ratio. If some other heat loss reference is available during the day, then the diurnal variation of the downward solar flux relative to the reference will produce a clear signature that can be used to determine both k_c and k_b. This works best if the heat flux is relatively constant and comparisons with the reference can be made during preceding and following nights to make any needed relative calibration adjustments. Under partly cloudy skies, it is possible to use clouds as direct solar beam choppers. The relative response of clear and black sensors to cloud interruptions then determines the k_c/k_b ratio directly, provided that the heat flux varies relatively slowly compared to the duration of a cloud interruption. This method is demonstrated in Part II. It is also possible to use this method to obtain response ratios in the presence of haze or thin cirrus clouds, conditions which would not allow a calibration of absolute values for the solar responsivities.

It is important to note that true calibration in the field requires support from independent measurements of the net solar flux. Nevertheless, when such support is absent, one can obtain valuable checks on system performance using cloud modulations and solar irradiance models.

e. Data system design

The data collection and transmission systems are contained within the WOCE Lagrangian drifter buoy, a 16–in.-diameter sealed fiberglass and epoxy ball. Two connectors are provided: one for the float data, and a second for predeployment testing, programming, and control. The float signals are read and processed using a Campbell relay multiplexer and CR-10 datalogger, which also controls a Telonics ST-5 transmitter for communication with the Argos satellite data collection system. The data system reads clear and black sensor flux samples every 2 s and attaches a sign based on the reading of the orientation sensor. These signed samples are averaged for 20 min. Submergence-filtered averages are also computed for the same periods by excluding samples taken when submergence is indicated. The system also records fractional times of up-orientation (±5%) and submergence (±0.05%) for each 20-min period. All of these processed measurements are transferred to every transmit buffer. Skin, air, and bulk temperatures are sampled internally every minute and averaged over 20 min. But, because of limited Argos bandwidth, only a fraction of these are put into the transmit buffer: the skin temperature average is only collected once every two hours and the bulk temperature only once per hour. Other housekeeping information, including battery voltage, leakage resistance between sensor and water, and resistance of an internal water sensor are collected only one or two times per day. It takes 12 h of data collection to fill one transmit buffer. While one buffer is being transmitted, data for the next one are collected and processed.

The transmit buffer contains 288 words, organized into 18 frames of 16 words each. Each of the 18 frames contains a checksum that allows us to identify data points subsequently corrupted during the transmission process. Once the buffer is filled, it is transferred to the Telonics transmitter, which then transmits it for 12 h, one 16-word frame at a time, at a rate of one frame every 30–31 s. The National Oceanic and Atmospheric Administration's (NOAA) polar orbiting satellites (*NOAA-12* and *-14*) receive the data and provide a position fix on the drifter buoy, which is relayed back to the Argos service. Argos uses electronic mail to send the buffer contents to the user. It also has provided timely and accurate position data that enabled four successful recovery operations in the open ocean (twice in the Gulf Stream, once in the western Pacific, and once in the Greenland Sea). The electronics are powered by a 15-V battery consisting of two 7.5-V alkaline dry cells, providing continuous operation for approximately 4–6 months. The second connector on the drifter allows us to use external power for laboratory tests, provides for data readout without using the transmitter, and allows us to change the control program externally. Just prior to deployment the connector is fitted with a sealed cover that also provides a jumper that enables the transmitter.

5. Sensor characterization in a laboratory environment

Because the commercial sensor has a thermal resistance that differs from that of water and also blocks the

local viscous coupling, there is some question whether its measurements are representative of heat flow outside the float ring. A related issue is whether the mesh layers, in their alteration of the surface geometry, promote or inhibit sensible or latent heat transport, and whether the ring-shaped float has an aerodynamic effect that biases the heat flux measurements within the ring. Some of these issues were addressed in laboratory tests, as described in the following.

a. Responsivity and linearity tests

Laboratory responsivity measurements were carried out by comparing flux sensor readings with calorimetric flux measurements based on electrical substitution. The float assembly was placed in a shallow pan of water that was temperature-controlled to match the ambient temperature. The pan was isolated everywhere except at its surface, which was exposed to breezes of unsaturated air that promoted evaporative cooling. The electrical power needed to replace the surface heat loss, divided by the area of the exposed surface, gave us the average heat flux from the surface. We divided this flux into the SOHFI signal output to define the sensor's responsivity. This calibration method presumes that the average ventilation of the exposed surface is equal to the ventilation in the immediate vicinity of the flux sensor, an assumption that has been insufficiently investigated at this point.

Using a pan that was just large enough to contain the float assembly, Suomi et al. (1996) reported a close agreement between flux sensor measurements and the laboratory calorimetric measurements in the heat flux range of 120–340 W m^{-2}. Their sensor flux measurements were about 8% below the value expected from the manufacturer's calibration. The significance of this discrepancy and its origin are not understood, although it might easily be due to a nonuniformity in the ventilation of the exposed wet surface. Subsequent measurements have shown responses both above and below the manufacturer's calibration by comparable percentages. On the whole, these results show that the very local heat flux measurements of the thermopile sensors do a fair job of representing the average fluxes over at least the mesh-covered region.

Subsequent responsivity tests used a larger pan of water and added a water circulation system aimed at producing a better temperature uniformity. Results for two sensors of the Gulf Stream design (Fig. 6a) indicate at least crudely linear behavior up to rather large fluxes (up to 500 W m^{-2}). Deviations from linear response are indicated at higher flux levels, and evidence for a small offset is seen at low flux levels. These sensors, though tested in saltwater, did have drainage wires and produced droop-free responses. The small offset seen near 50 W m^{-2} appears to be a consequence of the forced tank circulation system and disappears when the tank circulation is turned off, as was the case for measurements of the Greenland Sea sensor design shown Fig. 6b. These latter results indicate good sensor-to-sensor consistency and show that the SOHFI flux sensors, when using the calibration of the flux plate manufacturer, do a good job of representing the average fluxes over the area of the calorimeter pan, except for a 20% shortfall at very high fluxes. The probable cause of the apparently reduced responsivity between 500 and 800 W m^{-2}, seen for both sensor designs, is a wind-induced forced convection that transfers heat more efficiently in the regions of open water than in the regions where water is covered by fiberglass mesh. This is discussed more thoroughly in a subsequent section. Nonuniformity of ventilation over the water surface might also affect these results to a noticeable degree. An important point to note is that there may not be much practical significance to this nonlinear characteristic because it seems to occur at flux

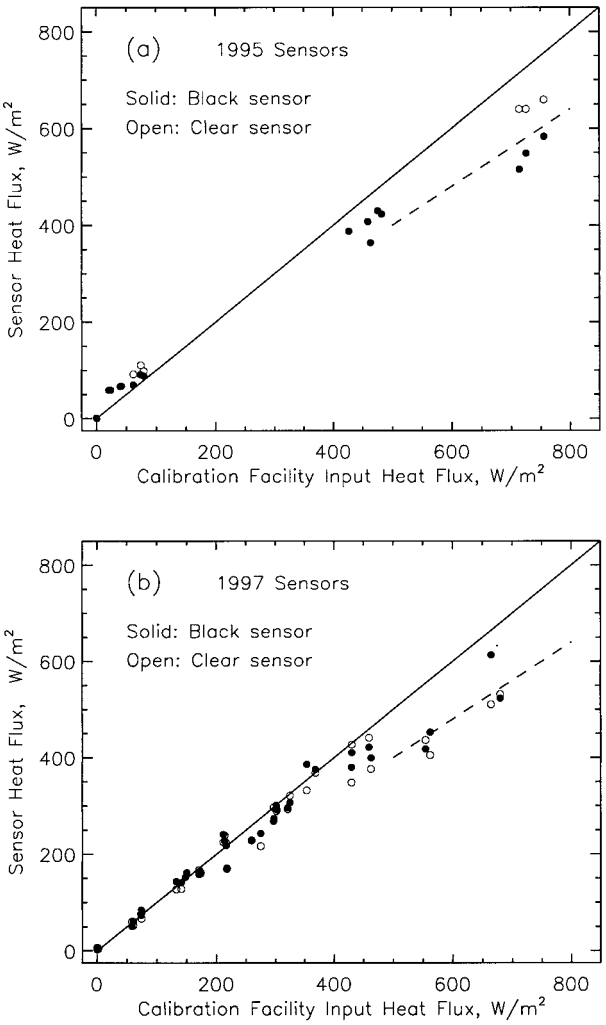

FIG. 6. Sensor response under laboratory conditions (a) for the Gulf Stream sensor configuration and (b) for the Greenland Sea sensor configuration. Sensor readings, using the manufacturer's calibration, are plotted against calorimetric measurements. The dashed reference lines are at 80% of the calorimetric response.

levels significantly beyond those observed in the field. Yet, if nonlinear behavior is associated more with wind speed than with flux level, it might become important in field observations, and thus needs to be better characterized.

In the laboratory, we have also observed responsivity differences associated with float orientation. It was not unusual to find 7% responsivity differences between top-up and top-down orientations. Because the thermopile sensor is inherently orientation insensitive, we must consider how the flux plate interacts with the rest of the float to find an explanation. As suggested in the previous discussion, it is possible that the response asymmetry is due to up–down differences in the way the mesh fibers are suspended over the flux plates, perhaps associated with a small curvature in the flux plate. An obvious orientation asymmetry has not been observed in field tests, perhaps because of masking by large natural variations in flux levels, or perhaps because the larger agitation of the mesh in field operation causes small displacements of fibers relative to the thermocouple junctions. In any case, the asymmetry seen in the laboratory needs to be further investigated before implementation of any countermeasures.

b. Offset characterization

Because the differential thermopile flux sensor has an inherently offset-free output, any appearance of offsets suggests a fault either in the signal electronics or in our calibration facility. While the Campbell CR-10 datalogger specifications do not provide a specific value for input offset, we have measured the overall system offsets using sensors within a covered calibration that forces a zero heat flux condition. With the Gulf Stream sensor design connected to the calibration facility data system, we measured offsets of 0.5–0.6 W m^{-2}, which is equivalent to preamp input voltage offsets of 0.18–0.22 μV. For the ruggedized sensors used in the Greenland Sea deployment, which have about 53% of the responsivity of the Gulf Stream sensors, this voltage offset is equivalent to a flux offset of about 1 W m^{-2}. However, field tests with that sensor design have yielded offsets about twice as large (2.4–3.8 W m^{-2}) and consistently negative, as compared to positive offsets seen with previous sensors. This unexpectedly large offset is thought to be a consequence of the low electronics temperatures during this deployment, with somewhat lower supply voltages a possible contributing factor. Laboratory environmental tests with a similar preamp show offsets of 2 μV at 0°C, which is equivalent to a flux offset of 10.5 W m^{-2}.

The much larger offset appearing at small nonzero flux levels in Fig. 6a is associated with the tank circulation system and is not present when the circulation system is turned off, as demonstrated in Fig. 6b.

c. Effects of fiberglass mesh on transports

To estimate what effect the fiberglass mesh had on the local heat flux, we compared servo power requirements with and without the heat flux sensor assembly in the calibration tank, using fairly large flux levels of about 800 W m^{-2} to obtain good signal-to-noise ratios. Accounting for the mesh area, float area, and tank area, and assuming uniform ventilation over all surfaces, we derived a heat loss over the mesh-covered region that was 0.86 $\pm$ 0.13 times that over the region of open water. This result, suggesting that the mesh depresses the local heat flux, is consistent with a less uncertain implication derived from surface temperature measurements made with a Barnes narrowbeam radiation thermometer. The emitting temperature within the mesh-covered region was found to be 1.5°C lower than in the open water. This implies a 9% reduction in saturation vapor pressure at the mesh surface. Assuming equal ventilation of the mesh surface and the open water, and an ambient relative humidity of 40 $\pm$ 10%, we find that the evaporative heat flux over the mesh is 0.81 $\pm$ 0.05 times that over the open water. These two results were obtained using methods that are completely independent of the flux plate sensor calibration. We also obtain a similar result by comparing the SOHFI flux measurements (using the flux plate calibration provided by the manufacturer) with the fluxes measured by the calorimeter system. In Fig. 6 we see that at relatively high flux levels, the SOHFI flux measurements fall about 20% below the calorimetric values.

These three independent results strongly imply that, under laboratory conditions, the mesh does reduce evaporative fluxes at high flux levels by about 20%. This is probably related to circulation currents within the pan of water that is used in the calorimeter system. Wind stress on the open water will undoubtedly induce a surface current that moves in the wind direction, either terminating or beginning at a tank boundary, where a vertical current must be generated to conserve mass flow. This may be considered analogous to the surface renewal process discussed by Liu and Businger (1975). The water surface within the mesh-covered region will not experience this stress because surface tension couples it to the mesh fibers. At high wind speeds, it is likely that the wind-driven currents will provide a forced convective transport of heat from the pan bottom to the water surface that is more efficient than the natural convection that otherwise operates. We speculate that the thermal conduction region is thinned sufficiently by this forced convective transport, in the open water regions, that the temperature difference required to replace the lost heat is reduced relative to that in the mesh-covered region. Under these conditions, the mesh-covered region appears to have a higher thermal resistance, requiring a larger temperature difference to transport the same heat. Also because evaporation is such a strong function

of temperature, this actually leads to a somewhat reduced evaporative heat flux.

However, because the flux depression seen in the laboratory appears only at relatively high flux levels, and because the boundary conditions created by the small tank might lead to quite different forced convective transports relative to open ocean conditions, it is not at all clear that this effect will have any significance under field measurement conditions. While current field results (Part II) provide some evidence for reduced sensitivity under heavy weather conditions, rather large uncertainties in field intercomparisons, as well as the possibility of inadequate submergence filtering as a contributing factor, prevent a definitive statement on this point. This is an area needing further investigation.

6. Discussion and conclusions

The relatively close agreement (within about 10%) between the skin-layer heat flux measurements and independent calorimetric measurements, up to moderately high flux levels, indicates that the net effect of heat flow perturbations by the flux plate and mesh is not so large as to prevent useful measurements. This might be explained by a compensation effect: even though the flux plate resistance might be significant compared to the skin resistance, there may be an adjustment of the temperature structure to maintain nearly the same heat flow in spite of the increased thermal resistance. The apparent 20% drop in responsivity seen at flux levels beyond 500 W m^{-2} seems to be caused by forced circulations set up within our laboratory water bath, and is more properly described as an enhancement of heat transport in the open water regions. It remains to be determined under what conditions similar effects are important in the ocean environment. Several anomalies in the test results seem to be more likely due to problems with our test setup, rather than a problem with the flux sensor or the basic method. Although some tests suggested small offsets at low flux levels, this anomaly is more likely a consequence of imperfect test conditions; both nonuniform ventilation and water circulation effects might have been contributing factors. Of course, the laboratory tests did not include the effects of waves on the flux measurements, and the general issue of performance in the field needs to be answered with field tests (preliminary results can be found in Part II).

Two adverse aspects of ocean operation were successfully addressed in the current design: 1) saltwater invasion of connectors and sensors was halted by changes in sensor fabrication methods and lead insulation design and 2) responsivity loss due to increased salt concentrations directly over the flux sensor was solved by providing channels for diffusion of the salt gradients. Additional design changes were made in the flux sensors to increase ruggedness, mainly to avoid costly patchwork repairs required to carry out laboratory checkouts prior to field deployments.

As described in Part II, field testing has partially verified SOHFI flux measurements by comparison with independent techniques, although the comparisons are of limited extent and thus not definitive. The major remaining problems that need to be addressed are 1) protection from seabird attacks and 2) correction for apparently reduced responsivity under high wind conditions. While we have approaches for dealing with both of these issues, they remain to be implemented and tested.

Acknowledgments. This research was partially supported by NSF Grants ATM-9419535 and ATM-92216065 through the NSF Physical Meteorology Program, directed by Ronald Taylor, and by the University of Wisconsin Space Science and Engineering Center (SSEC) directed by Francis Bretherton and Executive Director Robert Fox. We thank Gene Bucholtz, Nikola Ciganovich, Mike Dean, Robert Herbsleb, Robert Knuteson, Ronald Koch, Dennis McRae, Mark Mulligan, Robert Paulos, Henry Revercomb, Evan Richards, John Short, Jerry Sitzman, and Paul Wisniewski from SSEC, who contributed to the design, development, and field deployment efforts. We thank Frank Hines of RdF Corporation, Hudson, New Hampshire, for facilitating sensor design modifications and Myron Tanner of Campbell Scientific for assistance in data system programming. We also wish to acknowledge helpful detailed comments by the three anonymous reviewers.

REFERENCES

Black, R. G., and J. G. Holland, 1995: The boundary layer of Tropical Cyclone Kerry. *Mon. Wea. Rev.,* **123,** 2007–2028.

Blanc, T. V., 1983a: An error analysis of profile flux, stability and roughness length measurements made in the marine atmospheric surface layer. *Bound.-Layer Meteor.,* **26,** 243–267.

——, 1983b: A practical approach to flux measurements of long duration in the marine atmospheric surface layer. *J. Climate Appl. Meteor.,* **22,** 1093–1110.

Bradley, E. F., P. A. Coppin, and J. S. Godfrey, 1991: Measurements of sensible and latent heat flux in the western equatorial Pacific Ocean. *J. Geophys. Res.,* **96** (Suppl.), 3375–3389.

Businger, J. A., J. C. Wyngaard, Y. Izumi, and E. F. Bradley, 1971: Flux–profile relationships in the atmospheric surface layer. *J. Atmos. Sci.,* **28,** 181–189.

Charnock, H., 1955: Wind stress on a water surface. *Quart. J. Roy. Meteor. Soc.,* **81,** 639–640.

Defant, A., 1961: *Physical Oceanography.* Vol. 1, Pergamon, 729 pp.

Dobson, F., L. Hasse, and R. Davis, Eds., 1980: *Air–Sea Interaction: Instruments and Methods.* Plenum Press, 801 pp.

Donelan, M. A., 1990: Air–sea interaction. *The Sea: Ideas and Observations on Progress in the Study of the Seas,* Vol. 9, Part A, *Ocean Engineering Science,* B. Le Mehaute and D. Hanes, Eds., Wiley-Interscience, 239–292.

Downing, H. D., and D. Williams, 1975: Optical constants of water in the infrared. *J. Geophys. Res.,* **80,** 1656–1667.

Dyer, A. J., 1974: A review of flux profile relationships. *Bound.-Layer Meteor.,* **7,** 363–372.

Edson, J. B., A. A. Hinton, K. E. Prada, J. E. Hare, and C. W. Fairall, 1998: Direct covariance flux estimates from mobile platforms at sea. *J. Atmos. Oceanic Technol.,* **15,** 547–562.

Emanuel, K. A., 1986: An air–sea interaction theory for tropical

cyclones. Part 1: Steady-state maintenance. *J. Atmos. Sci.,* **43,** 585–604.

——, 1991: The theory of hurricanes. *Annu. Rev. Fluid Mech.,* **23,** 179–196.

Fairall, C. W., and S. E. Larsen, 1986: Inertial dissipation methods and turbulent fluxes at the air–ocean interface. *Bound.-Layer Meteor.,* **13,** 507–523.

——, J. B. Edson, S. E. Larsen, and P. G. Mestayer, 1990: Inertial-dissipation air–sea flux measurements: A prototype system using real-time spectral computations. *J. Atmos. Oceanic Technol.,* **7,** 425–453.

——, E. F. Bradley, D. P. Rogers, J. B. Edson, and G. S. Young, 1996: Bulk parameterization of air–sea fluxes for Tropical Ocean Global Atmosphere Coupled-Ocean Atmosphere Response Experiment *J. Geophys. Res.,* **101** (C2), 3747–3764.

Fleagle, R. G., and J. A. Businger, 1980: *An Introduction to Atmospheric Physics.* Academic Press, 432 pp.

Guymer, T. H., J. A. Businger, K. B. Katsaros, W. J. Shaw, P. K. Taylor, W. G. Large, and R. E. Payne, 1983: Transfer processes at the air–sea interface. *Philos. Trans. Roy. Soc. London,* **308 A,** 253–273.

Haussler, W., 1956: Ueber Temperatureprofile Beiderseits einer Verdunstenden Wasserflaeche. *Wiss. Z. Tech. Hochsch. Dresden,* **5,** 4356–450.

Hay, D. R., 1980: Fast-response humidity sensors. *Air–Sea Interaction: Instruments and Methods,* F. Dobson et al., Eds., Plenum Press, 413–432.

Hill, R. H., 1970: Laboratory measurements of heat transfer, wind velocity profiles, and temperature structure at an air–water interface. Rep. 7212, U.S. Naval Research Laboratory Washington, DC, 31 pp.

Khundzhua, G. G., A. M. Gusev, Ye. G. Andreyev, V. V. Gurov, and N. A. Skorokhvatov, 1977: Structure of the cold surface film of the ocean and heat transfer between the ocean and the atmosphere (English translation). *Atmos. Oceanic Phys.,* **13,** 506–509.

Kondo, J., 1975: Air–sea bulk transfer coefficients in diabatic conditions. *Bound.-Layer Meteor.,* **9,** 91–112.

Kraus, E. B., 1972: *Atmosphere–Ocean Interaction.* Oxford University Press, 275 pp.

——, and J. A. Businger, 1994: *Atmosphere–Ocean Interaction.* Oxford University Press, 362 pp.

Kuo, Y.-H., R. J. Reed, and S. Low-Nam, 1991: Effects of surface energy fluxes during the early development and rapid intensification of seven explosive cyclones in the western Atlantic. *Mon. Wea. Rev.,* **119,** 447–476.

Larsen, S. E., J. Hojstrup, and C. H. Gibson, 1980: Fast-response temperature sensors. *Air–Sea Interaction: Instruments and Methods,* F. Dobson et al., Eds., Plenum Press, 269–292.

——, J. B. Edson, C. W. Fairall, and P. G. Mestayer, 1993: Measurement of temperature spectra by a sonic anemometer. *J. Atmos. Oceanic Technol.,* **10,** 345–354.

Liu, W. T., and J. A. Businger, 1975: Temperature profile in the molecular sublayer near the interface of a fluid in turbulent motion. *Geophys. Res. Lett.,* **2,** 403–404.

——, K. B. Katsaros, and J. A. Businger, 1979: Bulk parameterization of air–sea exchanges of heat and water vapor, including the molecular constraints at the interface. *J. Atmos. Sci.,* **36,** 1722–1735.

Mammen, T. C., and N. von Bosse, 1990: STEP—A temperature profiler for measuring the oceanic thermal boundary layer at the ocean–air interface. *J. Atmos. Oceanic Technol.,* **7,** 312–322.

Masuda, K., T. Takashima, and Y. Takayama, 1988: Emissivity of pure and sea waters for the model sea surface in the infrared window. *Remote Sens. Environ.,* **24,** 313–329.

McAlister, E. D., and W. McLeish, 1969: Heat transfer in the top millimeter of the ocean. *J. Geophys. Res.,* **74,** 3408–3414.

Mitsuta, Y., and T. Fujitani, 1974: Direct measurement of turbulent fluxes on a cruising ship. *Bound.-Layer Meteor.,* **6,** 203–217.

Mollo-Christensen, E., 1979: Upwind distortion due to probe support in boundary layer observation. *J. Appl. Meteor.,* **18,** 367–370.

Ocean Observing System Development Panel, 1995: Scientific design for the common module of the Global Ocean Observing System and the Global Climate Observing System: An ocean observing system for climate. Department of Oceanography, Texas A&M University, 265 pp. [Available from Dr. Worth D. Nowlin Jr., Department of Oceanography, Texas A&M University, College Station, TX 77843-3146.]

Ortolano, D. J., and F. F. Hines, 1983: A simplified approach to heat flow measurement. *Adv. Instrum.,* **38,** 1449–1456.

Paulson, C. A., and T. W. Parker, 1972: Cooling of a water surface by evaporation, radiation, and heat transfer. *J. Geophys. Res.,* **77,** 491–495.

——, and J. J. Simpson, 1981: The temperature difference across the cool skin of the ocean. *J. Geophys. Res.,* **86** (C11), 11 044–11 054.

Payne, R. E., 1972: Albedo of the sea surface. *J. Atmos. Sci.,* **29,** 959–970.

Sanders, F., and J. Gyakum, 1980: Synoptic-dynamic climatology of the ''bomb.'' *Mon. Wea. Rev.,* **108,** 1589–1606.

Schluessel, P., W. J. Emery, H. Grassl, and T. Mammen, 1990: On the bulk skin temperature difference and its impact on satellite remote sensing of sea surface temperature. *J. Geophys. Res.,* **95** (C8), 13 341–13 356.

Schotanus, P., F. T. M. Nieuwstadt, and H. A. R. de Bruin, 1983: Temperature measurement with a sonic anemometer and its application to heat and moisture fluxes. *Bound.-Layer Meteor.,* **26,** 81–93.

Sromovsky, L. A., J. R. Anderson, F. A. Best, J. P. Boyle, C. A. Sisko, and V. E. Suomi, 1999: The Skin-Layer Ocean Heat Flux Instrument (SOHFI). Part II: Field measurements of surface heat flux and solar irradiance. *J. Atmos. Oceanic Technol.,* **16,** 1239–1254.

Stull, R. B., 1988: *An Introduction to Boundary Layer Meteorology.* Kluwer Academic Publishers, 666 pp.

Suomi, V. E., L. A. Sromovsky, and J. R. Anderson, 1996: Measuring ocean–atmosphere heat flux with a new in-situ sensor. Preprints, *Eighth Conf. on Air–Sea Interaction and Conf. on the Global Ocean–Atmosphere–Land System (GOALS),* Atlanta, GA, Amer. Meteor. Soc., 38–42.

Sybrandy, A. L., and P. P. Niiler, 1991: The WOCE/TOGA SVP Lagrangian drifter construction manual. WOCE. Rep. 63, University of California, Scripps Institution of Oceanography, La Jolla, CA, 58 pp. [Available from Scripps Institution of Oceanography Library, Document Delivery Service, University of California, San Diego, La Jolla, CA 92093-0219.]

World Meteorological Organization, 1990: Scientific plan for the Global Energy and Water Cycle Experiment. World Climate Research Program Publ. 40 (WMO/TD 376), 83 pp.